Jan Pech

Spectral/hp elements in fluid structure interaction

In: Jan Chleboun and Pavel Kůs and Petr Přikryl and Miroslav Rozložník and Karel Segeth and Jakub Šístek (eds.): Programs and Algorithms of Numerical Mathematics, Proceedings of Seminar. Hejnice, June 21-26, 2020. Institute of Mathematics CAS, Prague, 2021. pp. 98–109.

Persistent URL: http://dml.cz/dmlcz/703105

Programs and Algorithms of Numerical Mathematics 20
J. Chleboun, P. Kůs, P. Přikryl, M. Rozložník, K. Segeth, J. Šístek (Eds.)
Institute of Mathematics of the Czech Academy of Sciences, Prague 2021

SPECTRAL/HP ELEMENTS IN FLUID STRUCTURE INTERACTION

Jan Pech

Institute of Thermomechanics of the Czech Academy of Sciences
Dolejškova 1402/5, 182 00 Praha 8, Czech Republic
jpech@it.cas.cz

Abstract: This work presents simulations of incompressible fluid flow interacting with a moving rigid body. A numerical algorithm for incompressible Navier-Stokes equations in a general coordinate system is applied to two types of body motion, prescribed and flow-induced. Discretization in spatial coordinates is based on the spectral/hp element method. Specific techniques of stabilisation, mesh design and approximation quality estimates are described and compared. Presented data show performance of the solver for various geometries in 2D from slowly moving cylinder to high speed flow around aerodynamic profiles.

Keywords: spectral/hp element method, fluid structure interaction, spectral vanishing viscosity

MSC: 65M70, 74F10, 76D05

1. Introduction

In this work, we study incompressible fluid flow influenced by motion of a rigid object inside a domain. The problem is connected with deformation of a computational mesh, formulation of the incompressible Navier-Stokes equations in general coordinates and realisation of the numerical scheme in a software library, which supports spectral/hp element approximations in spatial coordinates.

In the base of the applied method stays the high-order semi-implicit algorithm proposed in [5], which is widely used for numerical solution of the incompressible Navier-Stokes equations

$$\frac{\partial \mathbf{v}}{\partial t} + \mathbf{v} \cdot \nabla \mathbf{v} = -\nabla p + \nu \nabla^2 \mathbf{v} + \mathbf{f} \tag{1a}$$

$$\nabla \cdot \mathbf{v} = 0\,. \tag{1b}$$

In (1), $\mathbf{v} = (u, v)^{\mathrm{T}}$ is the velocity vector, p denotes the *kinematic pressure* and ν is the *kinematic viscosity*. The term $\mathbf{f}$ represents a general volumetric action, which acts in

DOI: 10.21136/panm.2020.10

presented results as a forcing term balancing the equation for testing the scheme/code performance on manufactured solutions or as a correction term representing the coordinate transformation in general formulation arising in the fluid-structure interaction (FSI) case. The FSI-solver is described in [11] and its implementation is available as a part of the open source library Nektar++ [1].

The paper describes in brief the specific features of the applied methods and presents aspects of two 2D simulations. Firstly, a flow-induced motion of a cylinder which interacts with low Reynolds number flow as a harmonic oscillator. The second case is an application to high speed flow problem connected with modelling of the flutter of turbine blades, where we combine advanced techniques developed for high order approximations.

2. Numerical methods

Spectral/hp elements combine accuracy and efficiency of global spectral method with geometrical flexibility of finite elements (or finite volumes), which comes from a decomposition of the computational domain Ω to elements Ω_e, $\Omega = \cup_{e=1}^{E} \Omega_e$. The expansion space $\mathcal{V}$ for representation of functions acting in the solved problem consists of piecewise polynomials of a sufficiently high degree N,

$$\mathcal{V} = \left\{ f | f \in \mathcal{C}^0(\Omega), f(\boldsymbol{\chi}_e(\boldsymbol{\xi})) \in \mathcal{P}_N(\Omega_{st}),\ e = 1, \ldots, E \right\}, \tag{2}$$

where $\boldsymbol{\chi}_e(\Omega_{st})$ represents mapping from *standard* element Ω_{st} to particular element Ω_e and $\boldsymbol{\xi}$ denotes local coordinates in Ω_{st}. The piecewise polynomial space adopts the $\mathcal{C}^0$ continuity property of traditional low-order finite element formulations. The 2D basis $\{\phi_{pq}(x,y)\}_{p,q=0}^{N}$ as used in this study, has the form of a tensor product $\phi_{pq}(x,y) = \phi_p(x)\phi_q(y)$ of 1D basis polynomials $\phi_p(x)$, $\phi_q(y)$. The 1D basis consists of modified Jacobi polynomials. The basis is hierarchic (the basis with the highest degree N contains a lower degree basis) and satisfies the $\mathcal{C}^0$ continuity over elemental boundaries (for further details we refer to [4]).

Within a single element, functions are expanded to finite series

$$f(x,y) \approx \sum_{p,q=0}^{N} \hat{f}_{pq} \phi_p(x) \phi_q(y)\,. \tag{3}$$

The basis functions are chosen such that for smooth functions ($\mathcal{C}^\infty(\Omega)$) the *expansion/spectral coefficients* $\hat{f}_{pg}$ have the asymptotical property of *exponential decay*. For efficient application of the spectral/hp elements we assume that approximated functions are smooth enough and used polynomial degree N is large enough to achieve the fast "asymptotical" spectral decay.

All results in this work were achieved on quadrilateral meshes with fixed uniform polynomial degree and using implementations from the open source Nektar++ project ([1]).

Temporal discretisation in transformed coordinates

The algorithm for temporal discretisation of the incompressible Navier-Stokes equations [5] is of velocity-correction type and splits the solution of the coupled system (1) to two steps, the pressure-Poisson equation with high-order Neumann boundary condition and the correction of velocity components. The algorithm is based on the backward difference formula (BDF) approximating $\partial\mathbf{v}/\partial t$ and possibly highly accurate solution of equations of the form

$$\left(\nabla^2 - \lambda\right) a = g_a \,,\ \lambda > 0 \,, \tag{4}$$

where $a \in \{u, v, p\}$ is always one of the variables and g_a is an appropriate source term as defined below. Following [3], where the scheme is analysed, we can write the velocity-correction as two steps:

$$\begin{aligned} \nabla p_{n+1} &= -\frac{\gamma\hat{\mathbf{v}}_{n+1} - \sum_{q=0}^{Q} \alpha_q \mathbf{v}_{n-q}}{\Delta t} - \nu\left(\nabla\times\nabla\times\mathbf{v}\right)^* + \mathbf{N}^* + \mathbf{f}^* \quad \text{in } \Omega \,, \\ \nabla\cdot\hat{\mathbf{v}}_{n+1} &= 0 \quad \text{in } \Omega \,, \\ \hat{\mathbf{v}}_{n+1}\cdot\mathbf{n} &= \mathbf{v}_{\mathcal{D}}\cdot\mathbf{n} \quad \text{on } \Gamma_{\mathcal{D}} \,. \end{aligned} \tag{5}$$

Applying divergence to eq. (5) we obtain the Poisson equation ($\lambda = 0$ in (4)) for p_{n+1}. Having p_{n+1}, we evaluate the intermediate, divergence-free velocity field $\hat{\mathbf{v}}_{n+1}$ which acts on the right hand side of the second, velocity-correction step

$$\begin{aligned} \mathbf{L}(\mathbf{v}_{n+1}) - \frac{\gamma_0}{\nu\Delta t}\mathbf{v}_{n+1} &= -\frac{\hat{\mathbf{v}}_{n+1}}{\nu\Delta t} - \left(\nabla\times\nabla\times\mathbf{v}\right)^* \quad \text{in } \Omega \,, \\ \mathbf{v}_{n+1} &= \mathbf{v}_{\mathcal{D}} \quad \text{on } \Gamma_{\mathcal{D}} \,, \\ \frac{\partial\mathbf{v}_{n+1}}{\partial\mathbf{n}} &= \mathbf{v}_{\mathcal{N}} \quad \text{on } \Gamma_{\mathcal{N}} \,. \end{aligned} \tag{6}$$

In the equations above we denote $\mathbf{N} = -\mathbf{v}\cdot\nabla\mathbf{v}$, $\mathbf{L}(\mathbf{v}) = \nabla^2\mathbf{v}$, asterisk in superscript denotes extrapolation, $\mathbf{N}^* = \sum_{q=0}^{Q}\beta_q[\mathbf{v}\cdot\nabla\mathbf{v}]_{n-q}$ while subscript denotes the value at a particular time step, $\mathbf{v}_n = \mathbf{v}(t_0 + n\Delta t)$, α_q are coefficients of the BDF, $\Gamma_{\mathcal{D}}$ and $\Gamma_{\mathcal{N}}$ are boundaries with Dirichlet and Neumann condition for velocity.

Performance illustration of the second order scheme ($Q = 2$) as applied to problem with manufactured solution, which is smooth and bounded ($\Omega = [0, 2] \times [-1, 1]$, $u = 2\cos(\pi x)\cos(\pi y)\sin(t)$, $v = 2\sin(\pi x)\sin(\pi y)\sin(t)$, $p = 2\sin(\pi x)\sin(\pi y)\cos(t)$) is in Fig. 1.

The formulation in a general coordinate system as one of those variants proposed in [11] keeps the form of (5) and (6) while differences are only in generalisation of differential operators and the forcing term $\mathbf{f}$. The two-step formulation considering

transformation between Cartesian $(\bar{x}, \bar{y})$ and transformed coordinates (x, y) is then

$$\begin{aligned}
\nabla p_{n+1} =& J\Bigg[-\frac{\gamma\hat{\mathbf{v}}_{n+1} - \sum_{q=0}^{Q}\alpha_q \mathbf{v}_{n-q}}{\Delta t} \\
&- \nu\nabla\left(\frac{\mathbf{v}}{J}\cdot\nabla J\right)^* - \nu\left(\nabla\times\nabla\times\mathbf{v}\right)^* + \mathbf{N}^* + \mathbf{f}^*\Bigg] \quad \text{in } \Omega\,, \qquad (7)\\
\nabla\cdot\hat{\mathbf{v}}_{n+1} =& 0 \quad \text{in } \Omega\,,\\
\hat{\mathbf{v}}_{n+1}\cdot\mathbf{n} =& \mathbf{v}_{\mathcal{D}}\cdot\mathbf{n} \quad \text{on } \Gamma_{\mathcal{D}}\,,
\end{aligned}$$

where the identity $\nabla^2\mathbf{v} = \nabla(D(\mathbf{v})) - \nabla(\frac{\mathbf{v}}{J}\cdot\nabla J) - \nabla\times\nabla\times\mathbf{v}$ was used and $\mathbf{f}$ newly represents the difference between operators in Cartesian and transformed systems,

$$\mathbf{f} = \left[\bar{\mathbf{N}}(\mathbf{v}) - \mathbf{N}(\mathbf{v})\right] + \left[-\bar{\mathbf{G}}(p) + \frac{\nabla p}{J}\right] + \nu\left[\bar{\mathbf{L}}(\mathbf{v}) - \mathbf{L}(\mathbf{v})\right]\,. \qquad (8)$$

The bar above a symbol denotes operators formulated in transformed coordinates, e.g. $\bar{\mathbf{G}}(p) = g^{ij}p_{,j}$, where g^{ij} is the inverse of the metric tensor and subscript after a comma denotes a covariant derivative. Similarly, transformed divergence becomes $\mathcal{D}(\mathbf{v}) = \frac{1}{J}\nabla\cdot(J\mathbf{v})$ (for detail description we refer to [11]).

Similarly the correction step for velocity takes the form

$$\begin{aligned}
\mathbf{L}(\mathbf{v}_{n+1}) - \frac{\gamma_0}{\nu\Delta t}\mathbf{v}_{n+1} &= -\frac{\hat{\mathbf{v}}_{n+1}}{\nu\Delta t} - \nabla\left(\frac{\mathbf{v}}{J}\cdot\nabla J\right)^* - \left(\nabla\times\nabla\times\mathbf{v}\right)^* - \mathbf{f}^*\,,\\
\mathbf{v}_{n+1} &= \mathbf{v}_{\mathcal{D}} \quad \text{on } \Gamma_{\mathcal{D}}\,, \qquad (9)\\
\frac{\partial\mathbf{v}_{n+1}}{\partial\mathbf{n}} &= \mathbf{v}_{\mathcal{N}} \quad \text{on } \Gamma_{\mathcal{N}}\,,
\end{aligned}$$

which is again a form of (4). Algorithm (7)–(9) and its implementation in the Nektar++ library followed solely the work of Serson [11].

Spectral vanishing viscosity and dealiasing

Spectral and high-order methods are connected with attempts for full resolution of solutions ([10]). However, there are plenty of situations, in which sufficiently accurate approximations are still far from being achievable. If the highest accuracy is not necessarily needed, techniques of *spectral vanishing viscosity* (SVV) may be used to improve performance of the scheme through stabilisation. Technique of Exponential, Power or DG (Discontinuous Galerkin) kernels of SVV are available (for detail description we refer to [6], [7]). The SVV technique manipulates the expansion coefficients of poorly resolved solution to suppress energy in the highest order modes, however, if spectral convergence is achieved, the SVV brings a limit of accuracy. This illustrates Fig. 1, where we compare the temporal convergence of the IMEX scheme for the direct method and three versions of the SVV kernel. From this comparison we conclude that SVV with Exponential kernel has the mildest impact on solution accuracy and therefore we use it in later simulations.

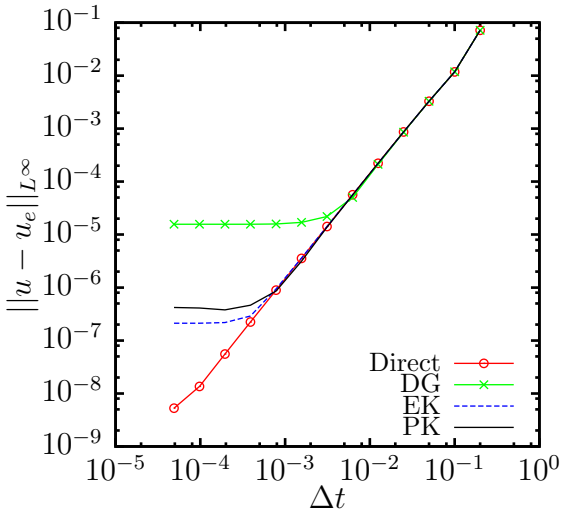

Figure 1: L^∞ norm of error between exact u_e and calculated u solution (x component of velocity) as dependence on timestep Δt. Data obtained using the second order IMEX scheme. Graphs compare the influence of SVV kernels (*EK*-exponential kernel, *PK*-power kernel, *DG*-DG kernel, *Direct*-no SVV).

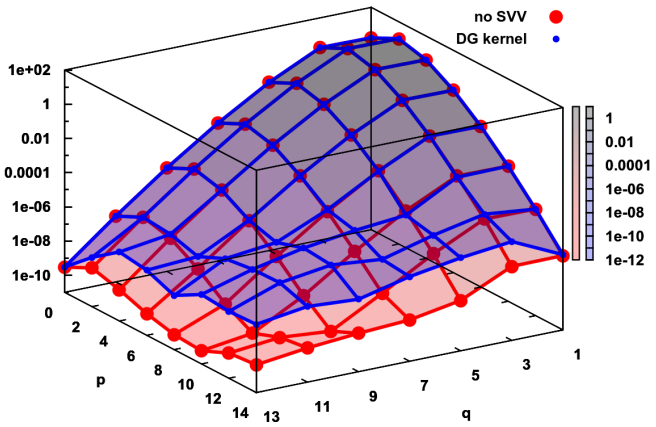

Figure 2: Exponential convergence of expansion (spectral) coefficients $\hat{f}_{pq}$ in a single element with expansion degree 14. Comparison between spectrum obtained without SVV technique (red, "no SVV") and SVV with DG kernel (blue, "DG"). Values of the highest degree modes provide an estimate of the approximation error.

Accuracy limit presented by SVV as observed in the temporal convergence is also directly visible from convergence of expansion coefficient spectra, see Fig. 2. The coefficients of the highest expansion modes provide us with a very efficient tool for estimate of achieved accuracy in spatial coordinates.

Another technique which improves the computational stability is *dealiasing*. It increases the number of quadrature points by 3/2 to keep accurate numerical integration of quadratic terms, e.g. the convection $\mathbf{v} \cdot \nabla \mathbf{v}$. It improves the quality of evaluation of the expansion coefficients. However, its impact is observable only for very unresolved problems, since it is under the truncation error if the spectral convergence is achieved (see e.g. [8]).

3. High degree simulation of moving cylinder

The first of the studied problems demonstrates performance of the high degree approximation in FSI. The approach considers decomposition of the computational domain to a minimal number of elements and using very high degree polynomials instead. As Fig. 3 illustrates, we divided the domain to 9 elements only. Large elements forming the boundary of the cylinder were deformed appropriately and with sufficient precision.

Solutions were calculated with expansion degree $N = 50, 60, 70, 80$. Parallelisation using 9 cores was employed, so each core was dedicated to one element. Each of the parallel processes used relatively large amount of memory, accordingly to the used polynomial degree. Such approach is in contrast to parallelisation strategies on graphics cards characterised by a huge amount of cores with small memory. Current tests confirmed the observation from [8], where maximum number of modes, 97, was determined to be available if the double precision representation of real numbers is used. This limitation arises from finite precision representation of quadrature formulas. The limit was observed if spectral dealiasing technique was used for the highest order approximations as it increases number of quadrature points by a factor 3/2. With dealiasing, the number of modes was limited to 65, what coincides very well with 97 modes/quadrature points without dealiasing. Motion of the cylinder was described by equation of a driven harmonic oscillator

$$m\frac{\mathrm{d}^2x}{\mathrm{d}t^2} + c\frac{\mathrm{d}x}{\mathrm{d}t} + kx = f_d \tag{10}$$

for both spatial directions independently. Depending on constants of mass m, "spring" constant k and damping c, the motion leads to overdumped, critically dumped or underdumped regime. The aerodynamic forces acting on the moving body define the driving forces f_d in (10). Initially underdumped regime develops to critically dumped, when the cylinder motion is balanced by vortex shedding and resistance of the fluid. Characteristics of the cylinder motion can not be estimated a priori and the computation failed if the cylinder motion achieved larger displacements or motion velocities.

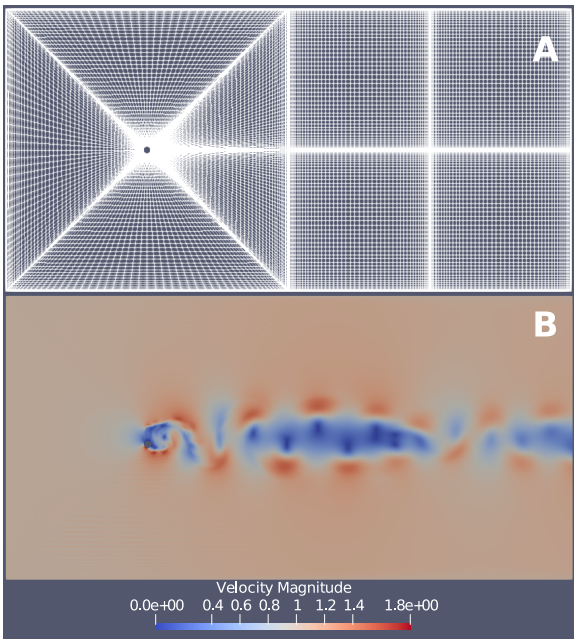

Figure 3: A: Computational mesh for simulation of flow around cylinder and FSI. White lines connect points of the Gauss-Legendre-Lobatto quadrature of order 50. These points are denser towards element boundaries. Mesh consists of 9 elements only. B: Field of velocity magnitude for moving cylinder do not resemble von Karman vortex street of static cylinder (number of modes was 80, cylinder is cca 1 diameter below the original position at this instance of time.)

The high order pressure boundary condition ([5], [11]) was prescribed on boundaries where Dirichlet condition for velocity was set. Boundary conditions for velocity were no-slip on cylinder wall, constant Dirichlet on inlet, top and bottom side and homogeneous Neumann on outflow. This choice of boundary conditions leads to non-smooth solutions, with singular points at inlet-boundary-side corners of Ω. This is obvious since equation of the type $(\nabla^2 - \lambda)u = f$ is solved with constant boundary values while domain boundary is not smooth. For this reason spectral accuracy could not be achieved for any polynomial degree, however the simulation was stable for the limited cylinder motion despite very high polynomial degree (up to 80). The flow regime was set to $\mathrm{Re} = 150$ what is very closely above the transition to three-dimensionality of the flow around cylinder (c.f. [9]), often denoted as the onset of turbulence. A full three-parameter study of ranges for m, k and c is beyond the scope of this work, we present the velocity field for $m = 3.14$, $k = 61.92$ and $c = 0.2$ as an illustration in Fig. 3.

4. Blade cascade flow

As the second FSI case, we studied a model of incompressible fluid flow in geometrically simplified blade cascade consisting of five flat blades with edges of circular profile. The central blade had a rotational degree of freedom and it was vibrating with prescribed frequency of 5Hz and amplitude of the angle of attack $\pm 5°$. Computational mesh consisted of approx. 19000 quadrilateral elements. Polynomial degree 6 was set for the velocity components, while degree 5 was prescribed for pressure, the timestep was always set to $\Delta t = 1e-5$. The top and the bottom of the computational domain simulated walls of the measuring section in a wind tunnel. Therefore, it carried, as well as the blades, the no-slip boundary condition, $\mathbf{v} = (0,0)^{\mathrm{T}}$. The computational mesh was condensed towards these domain-boundaries, where the turbulent boundary layer occurs. The inlet boundary condition was constant velocity profile while the robust outflow boundary condition proposed in [2] was used on the downstream boundary. The Reynolds number related to the blade chord was relatively high, $\mathrm{Re} = 1178100$, what necessarily leads to stability problems of the directly applied IMEX scheme. This implies a very short time step. Instead of shortening the time-step, we applied the SVV technique. The impact of various SVV kernels to the solution and final data illustrates Fig. 4, where the central blade of the cascade was rotated with a static angle. It should be noted that the drag force F_x is that quantity in which the data exhibit the largest discrepancies.

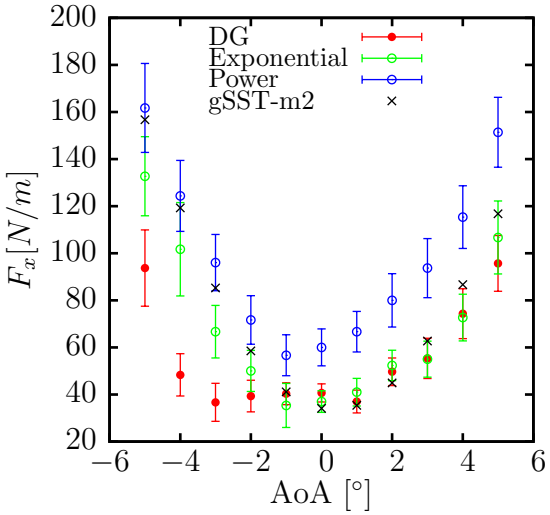

Figure 4: Drag force acting on the central blade in the blade cascade for various static angles of attack, AoA. Comparison of influence of various SVV kernels (DG kernel, Exponential and Power kernel) to the solution and comparison with results achieved by stationary finite volume solver combined with turbulence SST model.

The velocity field represented very small, quickly moving vortical structures in boundary layer areas of all blades and wake region, see Fig. 5. Output data were therefore oscillatory (see Fig. 6) and final single values were obtained by averaging data over time. Errorbars in Fig. 4 then show the standard deviation from the average for various static angles.

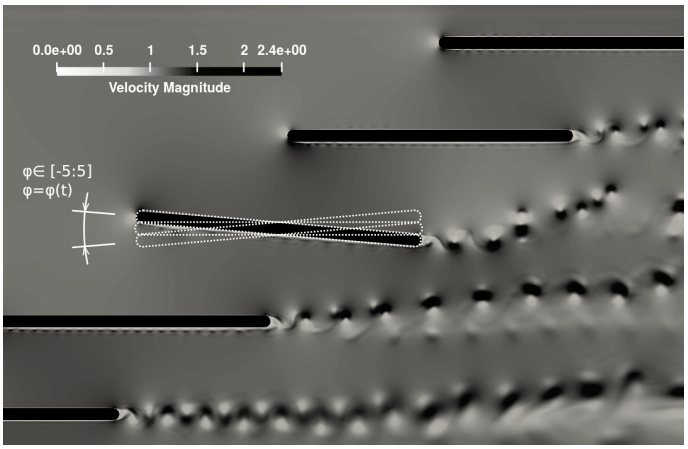

Figure 5: Detail of instant velocity magnitude field in area of the central, rotationally vibrating, blade of flat profile. The central blade changes position rotationally as indicated by dashed lines.

Fig. 6 shows evolution of forces acting on the surface of the central blade in the vertical direction, F_y is represented by the lift coefficient $C_L = 2F_y/(c\rho U^2)$ (blade chord $c = 0.12\,\mathrm{m}$, density $\rho = 1.21\,\mathrm{kgm}^3$, inlet velocity $U = 166\,\mathrm{ms}^{-1}$). Scattering of the graphs in this figure does not represent numerical noise. In a detail view, the curves are smooth and reflecting existence of small structures inside the boundary layer.

Finally, we present an insight to convergence of expansion coefficients in Fig. 7. Plotted values are obtained as a sum of two highest mode expansion coefficients belonging to all elemental boundaries. This visualisation of solution approximation quality gives an instant estimate of truncation error without additional computational costs and can be used as a tool for mesh and polynomial degree optimisation.

5. Conclusion

Spectral/hp element method is well developed today and prepared for advanced, geometrically complex, problems of engineering. Available codes come with features allowing high performance computing on the cutting edge of research. The method brings important features for applications such as the suppression of numerical diffusion, a significant decrease of degrees of freedom in the algebraic system and an insight to spectra of expansion coefficients, which gives a cheap estimate of quality of spatial approximation of the solution.

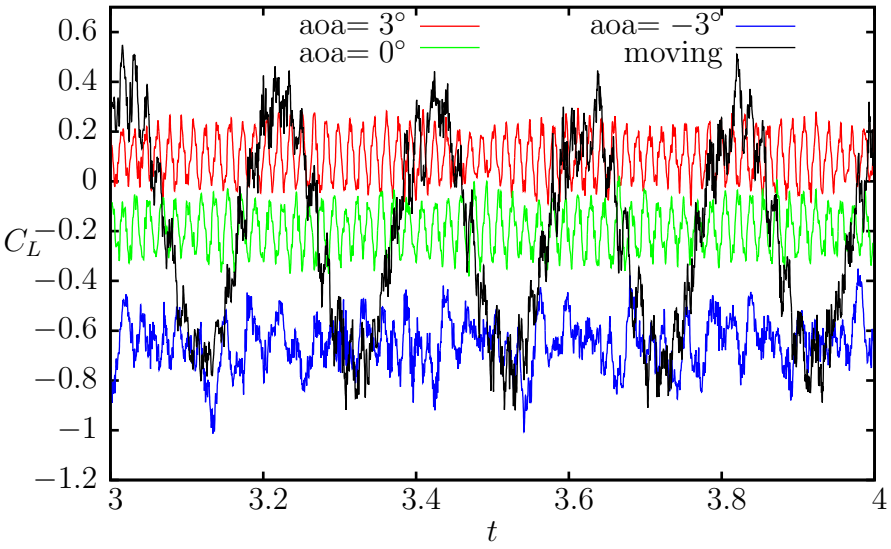

Figure 6: Time evolution of lift coefficient for one rotationally vibrating blade in blade cascade (*moving*) compared to statically rotated cases with angle of attack 3°, 0° and −3° (*aoa*= 3°, *aoa*= 0°, *aoa*= −3°). The vibrating blade rotates with amplitude ±3° and frequency 5Hz.

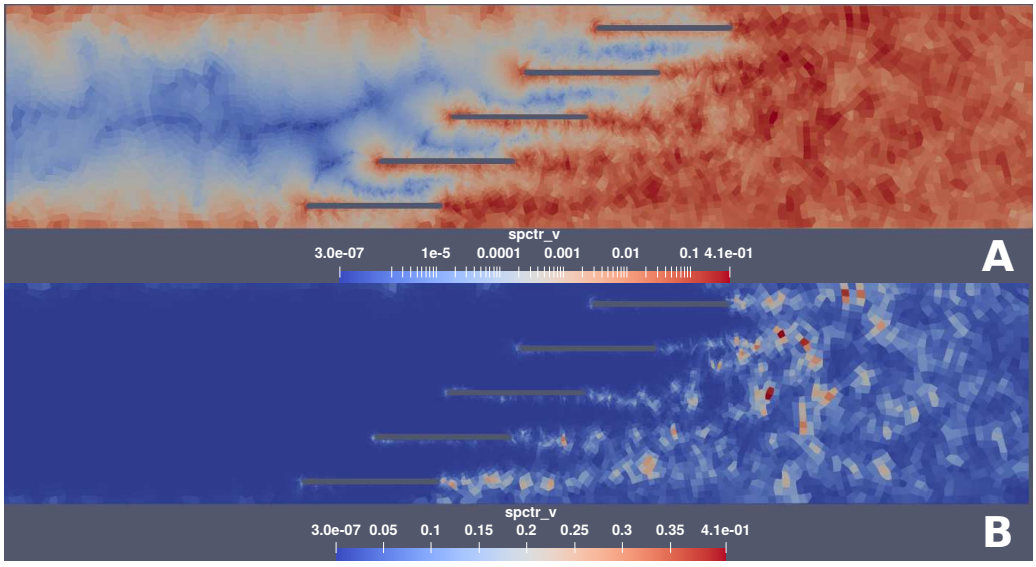

Figure 7: Maps illustrating achieved convergence in spectra of y-component of velocity v. A: logarithmic coloring shows regions of lower quality of approximation. B:linear coloring discovers particular elements of lower quality.

Presented results have also shown some limiting factors, as is the highest polynomial degree which can be used in double precision representation of real numbers in common computers. Simulation of incompressible flow, which corresponds to Mach number 0.5 is beyond the limit of the model, but the scheme taking advantage of the SVV technique was proved to be very robust despite rapidly developing structures with steep spatial gradients in the flow field. For more, obtained results are comparable with classical finite volume computations using turbulent models. In contrast to low order methods, fast convergence of expansion coefficients (spectral accuracy) may be achieved, and the method still does not appear to be exhausted. Analysis of spectral convergence in particular elements may be used as an indicator for automatic improvement or optimisation of mesh and applied polynomial degree. Limitation to 2D simulations in this work is one of the aspects, which is obviously insufficient for proper modelling of real flows and is left for further research activity.

Acknowledgements

The work was supported by the Czech Academy of Sciences, project MSM100761901. The support of the Czech Science Foundation (GACR) under grant no. 20-11537S is also gratefully acknowledged.

References

[1] Cantwell, C. et al.: Nektar++: An open-source spectral/hp element framework. Computer Physics Communications **192** (2015), 205–219.

[2] Dong, S., Karniadakis, G., and Chryssostomidis, C.: A robust and accurate outflow boundary condition for incompressible flow simulations on severely-truncated unbounded domains. Journal of Computational Physics **261** (2014), 83–105.

[3] Guermond, J.L. and Shen, J.: Velocity-correction projection methods for incompressible flows. SIAM Journal on Numerical Analysis **41** (2003), 112–134.

[4] Karniadakis, G. and Sherwin, S.: *Spectral/hp Element Methods for Computational Fluid Dynamics: Second Edition*. Numerical Mathematics and Scientific Computation, OUP Oxford, 2005.

[5] Karniadakis, G. E., Orszag, S. A., and Israeli, M.: High-order splitting methods for the incompressible Navier-Stokes equations. Journal of Computational Physics **97** (1991), 414–443.

[6] Kirby, R. M. and Sherwin, S. J.: Stabilisation of spectral/hp element methods through spectral vanishing viscosity: Application to fluid mechanics modelling. Computer Methods in Applied Mechanics and Engineering **195** (2006), 3128–3144.

[7] Moura, R., Sherwin, S., and Peiró, J.: Eigensolution analysis of spectral/hp continuous Galerkin approximations to advection-diffusion problems: Insights into spectral vanishing viscosity. Journal of Computational Physics **307** (2016), 401–422.

[8] Pech, J.: *Numerical modeling of unstable fluid flow past heated bodies*. Ph.D. thesis, Mathematical Institute of Charles University, 2016.

[9] Pech, J.: Laminar-turbulent transition in view of flow separation from isothermal and heated cylinder. In: D. Šimurda and T. Bodnár (Eds.), *Topical Problems of Fluid Mechanics 2020*. (2020), pp. 168–175.

[10] Posdziech, O. and Grundmann, R.: A systematic approach to the numerical calculation of fundamental quantities of the two-dimensional flow over a circular cylinder. Journal of Fluids and Structures **23** (2007), 479–499.

[11] Serson, D., Meneghini, J., and Sherwin, S.: Velocity-correction schemes for the incompressible Navier–Stokes equations in general coordinate systems. Journal of Computational Physics **316** (2016), 243–254.